LETTER

Arylammonium-Assisted Reduction of the Open-Circuit Voltage Deficit in Wide-Bandgap Perovskite Solar Cells: The Role of Suppressed Ion Migration

Cong Chen, Zhaoning Song,* Chuanxiao Xiao, Rasha A. Awni, Canglang Yao, Niraj Shrestha, Chongwen Li, Sandip Singh Bista, Yi Zhang, Lei Chen, Randy J. Ellingson, Chun-Sheng Jiang, Mowafak Al-Jassim, Guojia Fang, and Yanfa Yan*

ACCESS | 📊 Metrics & More | 📰 Article Recommendations | 🆂🅸 Supporting Information

ABSTRACT: Surface treatment using large alkyl/aryl ammonium cations has demonstrated reduced open-circuit voltage (V_{OC}) deficits in perovskite solar cells (PSCs), but the origin of the improvements has been vaguely attributed to defect passivation. Here, we combine microscopic probing of the local electrical properties, thermal admittance spectroscopic analysis, and first-principles calculations to elucidate the critical role of arylammonium interface layers in suppressing ion migration in wide-bandgap (WBG) PSCs. Our results reveal that arylammonium surface treatment using phenethylammonium iodide increases the activation energy barrier for ion migration on the surface, which suppresses the accumulation of charge defects at surface and grain boundaries, leading to a reduced dark saturation current density in WBG PSCs. With device optimization, our champion 1.73 eV PSC delivers a power conversion efficiency of 19.07% with a V_{OC} of 1.25 V, achieving a V_{OC} deficit of 0.48 V.
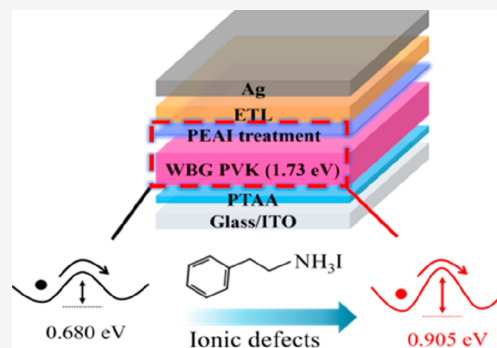
Perovskite solar cells (PSCs) have attracted a tremendous amount of attention in the past decade because of the superb photovoltaic properties of metal halide perovskites and the high certified power conversion efficiency (PCE) of single-junction devices that has already reached 25.2%.[1] Beyond single-junction PSCs, the bandgap tunability of perovskite materials ranging from ∼1.2 to 3 eV enables the realization of perovskite-based tandem solar cells, which have the potential to surpass the Shockley−Queisser (S−Q) thermodynamic limit of single absorber solar cells.[2−5] Perovskite-based tandem solar cells have made considerable progress in recent years.[6−18] Impressively, a variety of perovskite−silicon (Si),[6,15−17] perovskite−copper indium gallium diselenide (CIGS),[9,11] and perovskite−perovskite tandem solar cells have demonstrated PCEs of ∼25% or higher.[13,14] These achievements show the enormous potential of perovskite-based tandem solar cells in the future.[5] Notably, all of the tandem cells share a common component that is a top cell based on a wide-bandgap (WBG) (∼1.7−1.9 eV) perovskite absorber layer,[19−27] which plays a critical role in highly efficient tandem solar cells.

The performance of WBG PSCs has always been limited by a high open-circuit voltage (V_{OC}) deficit, which is defined as $\frac{E_g}{q} - V_{OC}$, where E_g is the bandgap of the absorber layer and q is the unit charge. PSCs based on WBG perovskites with a bandgap of >1.72 eV typically exhibit V_{OC} deficits (>0.5 V) that are larger than those of their lower-bandgap counterparts (Figure S1 and Table S1). While the origins of the large V_{OC} deficit in WBG PSCs are still under debate, it is certain that the shortfall is related to the composition of perovskites with a relatively high content of Br and Cs, which typically results in phase segregation and a relatively high defect density.[28,29] In particular, the aggregation of I-rich and Br-rich domains lowers the optical bandgap of WBG perovskites (that is primarily

determined by the lower bandgap of the domains in the material),[30−32] severely limiting the V_{OC} and thus the PCE of WBG PSCs. Therefore, strategies for mitigating large V_{OC} deficits in WBG PSCs are urgently needed to advance perovskite tandem solar cells.

Over the past few years, many approaches, such as compositional, additive, solvent, processing, and interface engineering techniques, have been employed to fabricate high-quality WBG perovskite films and devices.[19−27,33−36] Among them, bulk incorporation or surface treatment using large alkyl/aryl ammonium cations has been demonstrated to be most effective in reducing V_{OC} deficits of PSCs regardless of the perovskite composition. Despite the advances, the underlying mechanism of the alkyl/aryl ammonium treatment has always been attributed vaguely to a reduced defect density and increased carrier lifetime. In particular, little is known about the subtle differences in how the alkyl/aryl ammonium surface passivation affects WBG (>1.7 eV) and medium-bandgap (1.5−1.7 eV) iodine-based perovskites differently. Further efforts are needed to understand the origins and mechanisms of the large V_{OC} deficit in WBG PSCs and to explore effective strategies for mitigating this issue.

Very recently, we demonstrated an approach for probing the activation energy of ion migration in the perovskite absorber using a capacitance-based measurement,[37] which enables the PSC device performance analysis from the perspective of the ionic behavior in the perovskite absorber. Here, we combine the microscopic probing of localized electrical properties, thermal admittance spectroscopy (TAS) measurements, and first-principles calculations of defect migration to elucidate the primary factors limiting the V_{OC} in WBG PSCs. Our results reveal that, in contrast to the passivated grain boundaries (GBs) in the pure iodine-based perovskite, the nature of the relatively more conductive GBs than grain interiors (GIs) in WBG perovskite films fundamentally limits the V_{OC} of WBG PSCs. Our measurements and calculation consistently show that an arylammonium surface formed by phenethylammonium iodide (PEAI) increases the activation energy barrier for ion diffusion and suppresses the accumulation of ionic defects on the perovskite surface and at GBs. Consequently, inverted 1.73 eV WBG PSCs show the V_{OC} improved from 1.16 to 1.25 V, yielding a V_{OC} deficit of <0.5 V. Using the arylammonium surface treatment, we obtained champion PCEs of 19.1% and 24.1% for single-junction WBG PSCs and four-terminal (4-T) all-perovskite tandem solar cells. Our work provides a better understanding of how arylammonium cations suppress ion migration in WBG perovskites and its importance in reducing large V_{OC} deficits and improving the performance of WBG PSCs.

To identify the primary limiting factors for the large V_{OC} deficit in WBG PSCs, conductive atomic force microscopy (c-AFM) was employed to analyze the microscopic electrical properties of our benchmark $FA_{0.8}Cs_{0.2}Pb(I_{0.7}Br_{0.3})_3$ WBG perovskite films deposited on poly(triarylamine) (PTAA)/indium tin oxide (ITO)/glass substrates. Note that $Pb(SCN)_2$ was incorporated into our WBG perovskite films as an additive to promote perovskite grain growth, as reported previously.[20] Figure 1a shows a c-AFM map of a control WBG perovskite film, which exhibits nonuniform grain sizes with a heterogeneous current distribution over different grains, indicating the formation of polycrystalline domains with different chemical phases and electrical conductivities. All of the c-AFM images in Figure 1 and the Supporting Information were taken with the
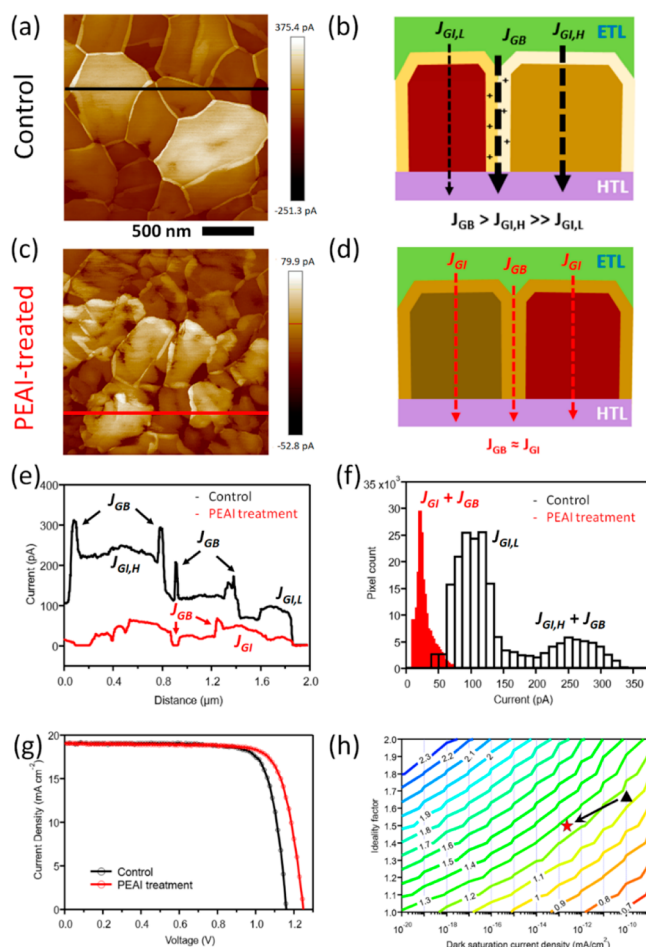
Figure 1. c-AFM images of (a) the control and (c) PEAI-treated WBG perovskite films. The scale bar is 500 nm. The images were flattened to show the best contrast. Schematic illustrations of current paths in (b) the control and (d) PEAI-treated WBG PSCs. (e) Line profiles of local current flow on the black and red lines in the c-AFM images of WBG perovskite films. (f) Histograms of the current distribution in the c-AFM images. (g) Light J−V curves of WBG PSCs without and with the PEAI treatment. (h) Contour plot of the theoretical V_{OC} as a function of dark saturation current densities and ideality factor. The triangle and star represent PSCs without and with the PEAI treatment, respectively.

same sample bias voltage (V_S) of +0.6 V to enable a reliable comparison. The segregation of I-rich and Br-rich (with respect to the 7:3 I:Br stoichiometry) domains leads to a distinct difference in the local electrical properties. The AFM tip (Pt-coated Si probe) forms primarily a junctionlike structure with the underlaying perovskite film. Dark saturation current J_0 of the structure is affected mainly by the perovskite bandgap. A larger current under the V_S indicates a larger J_0 caused by a smaller bandgap. The large grains, corresponding to the higher-contrast (brighter) grains in the c-AFM image (Figure 1a), are expected to be more conductive because their bandgaps are narrower than those with higher Br:I ratios and, therefore, allow higher local current flow ($J_{GI, H}$) through GIs. In contrast, the perovskite grains with a higher Br content tend to form smaller grains because Br accelerates the nucleation process, leading to a large number of small grains.[19] The Br-rich small grains, corresponding to the lower-contrast (darker) grains, are more electrically resistive, demonstrating lower

current flow ($J_{GI, L}$) through GIs. Therefore, the I-rich perovskite grains contribute larger dark currents (Figure 1b).

A remarkable heterogeneity in microscopic electrical behavior is discerned at the GBs of the WBG perovskite film in Figure 1a. The current signals at GBs (J_{GB}) are much higher than the current flows through GIs (J_{GI}), making GBs contribute to the increase in the leakage current in the WBG perovskites, as illustrated in Figure 1b. For comparison, we measured a conventional 1.55 eV MAPbI$_3$ perovskite film prepared using the same approach. In contrast to the WBG perovskite, the MAPbI$_3$ film (Figure S2) exhibits mostly resistive GBs, which indicates passivated GBs because of the PbI$_2$ passivation introduced by the addition of Pb(SCN)$_2$.[38] However, incorporating Pb(SCN)$_2$ into the WBG perovskites shows no efficacy in passivating GBs. For the FA/Cs-based WBG perovskite films, the dynamic of perovskite formation is greatly accelerated due to the presence of significant amounts of Cs and Br (20 and 30 mol % with respect to the monovalent cations and halide anions, respectively) in the precursor solution, leading to a higher density of defects.[19] The aggregation of the active ionic defects at GBs increases not only the electrical conductivity but also the extent of ion migration at the GBs.[39−42] Because Br has a higher vapor pressure and escapes more easily from GBs of perovskite, it is likely that mostly positively charged ions, such as halide vacancies and lead interstitials, accumulate on the surface and at GBs, introducing detrimental defect states and making GBs more electrically conductive.[43,44]

The ambiguity of the impact of conductive GBs or regions near GBs has been discussed in the literature[39,45−48] but deserves to be discussed further. The local current probed by c-AFM should be determined by two factors: the equivalent resistance of the probe−sample contact and the material resistivity of the local volume underneath the probe. If the contact resistance over the sample surface is uniform, the current contrast is determined by the local resistivity of the sample. A high J_{GB} is sometimes attributed to improved charge transport properties at the GBs, which can be beneficial for series resistance in a solar cell.[47,48] However, a current contrast in a c-AFM image is often dominated by the nonuniform electrical characteristics of the probe−sample contact. A substantially high J_{GB} value is typically detrimental because of the likelihood of concomitant high reverse leakage current in finished devices. The defective GB and defective surface and subsurface material would cause a higher current flow because of the increased J_0 of the probe−sample contact, which also results in an inferior leaking junction when the device is completed. Moreover, highly conductive GBs may indicate defective GBs without proper passivation, behaving as nonradiative recombination centers, significantly increasing the level of Shockley−Read−Hall (SRH) recombination. Therefore, the high current flows through the defective GBs, as probed by c-AFM, can substantially increase the macroscopic dark saturation current in a solar cell device, fundamentally limiting the photovoltaic performance of a device, particularly the V_{OC}. It is worth noting that some defective GBs show conductivities that are higher than those of the relatively conductive GIs that are formed due to the I−Br phase segregation, indicating that the defective GBs are likely to be the most critical factor contributing to the J_0 of a device.

To reduce the detrimental defects at the GBs of WBG perovskite films, we applied an arylammonium surface treatment using PEAI, which is known to be an effective two-dimensional perovskite passivation agent that has been demonstrated in some state-of-the-art PSCs.[33,49,50] We spin-coated 2 mg/mL PEAI in an isopropanol solution on as-prepared WBG perovskite films and performed the c-AFM measurement to identify the impact of PEAI on the microscopic electrical properties of the film (Figure 1c). Compared with the control film, the current flow through the perovskite grains is reduced by almost 1 order of magnitude, and the spatial distribution of microscopic conductivity becomes more uniform. Furthermore, there is an insignificant conductivity contrast between the GBs and GIs of the PEAI-treated film, indicating that J_{GB} is significantly reduced and comparable to J_{GI} (Figure 1d). Therefore, current flow through the perovskite film can be uniformly distributed across the GIs and GBs. The impacts of PEAI passivation on GIs and GBs are clearly displayed in the c-AFM line profile comparison in Figure 1e, where the PEAI treatment shows a marked effect in reducing the leakage current through both GBs (J_{GB}) and the grain interior (J_{GI}). Figure 1f compares the histograms of the microscopic current distribution in the control and PEAI-treated WBG perovskite films. The control WBG perovskite film exhibits two distinct local conductivity behaviors, including highly conductive GBs and GIs (J_{GB} and $J_{GI, H}$) and less conductive GIs ($J_{GI, L}$). In marked contrast to the control film, the film with the PEAI treatment shows a narrow distribution with a greatly suppressed average current of 26 pA, almost 1 order of magnitude lower than the average c-AFM current of 135 pA for the control film. Because the probe−perovskite contact in the c-AFM imaging qualitatively reflects the electrical aspect of the electron transport layer (ETL)−perovskite contact in a real solar cell, the microscopic current distribution in WBG perovskite films determines the macroscopic current flow in the corresponding devices. Suppressed local leaking current at GBs and the defective subsurface region of GIs is beneficial for reducing the overall dark saturation current density in the devices.

To reveal the influence of microscopic electrical properties on the macroscopic device performance of WBG PSCs, we fabricated solar cells with a glass/ITO/PTAA/FA$_{0.8}$Cs$_{0.2}$Pb-(I$_{0.7}$Br$_{0.3}$)$_3$/C$_{60}$/bathocuproine (BCP)/Ag structure (Figure S3). Figure 1g shows representative current density−voltage (J−V) curves of PSCs based on the control and PEAI-treated perovskite absorbers. With the PEAI treatment, V_{OC} increases significantly from 1.16 to 1.25 V, leading to an improvement in the PCE from 17.5% to 18.6%. To further understand the V_{OC} enhancement as a result of the PEAI treatment, in Figure 1f, we plot a V_{OC} contour of a general solar cell using the diode equation $V_{OC} = \frac{nkT}{q} \ln\left(\frac{J_L}{J_0} + 1\right)$, where n is the ideality factor, k is the Boltzmann constant, T is the temperature of a solar cell, and J_L and J_0 are the light and dark saturation current densities, respectively.

On the basis of the contour plot, for a solar cell with a given absorber layer bandgap and device operational temperature, V_{OC} is determined only by the combination of n and J_0. Note that n is not an independent variable but is strongly influenced by J_0. In reality, a small increase in n would typically lead to a significant increase in J_0 and, thus, a decreased V_{OC}. Therefore, from the perspective of device analysis, J_0 is an extremely critical parameter that determines the V_{OC} of a solar cell. A lower J_0 is desired to achieve a higher V_{OC} of a solar cell.

The light intensity-dependent device analysis shows the ideality factor n decreases from 1.69 for the control to 1.45 for
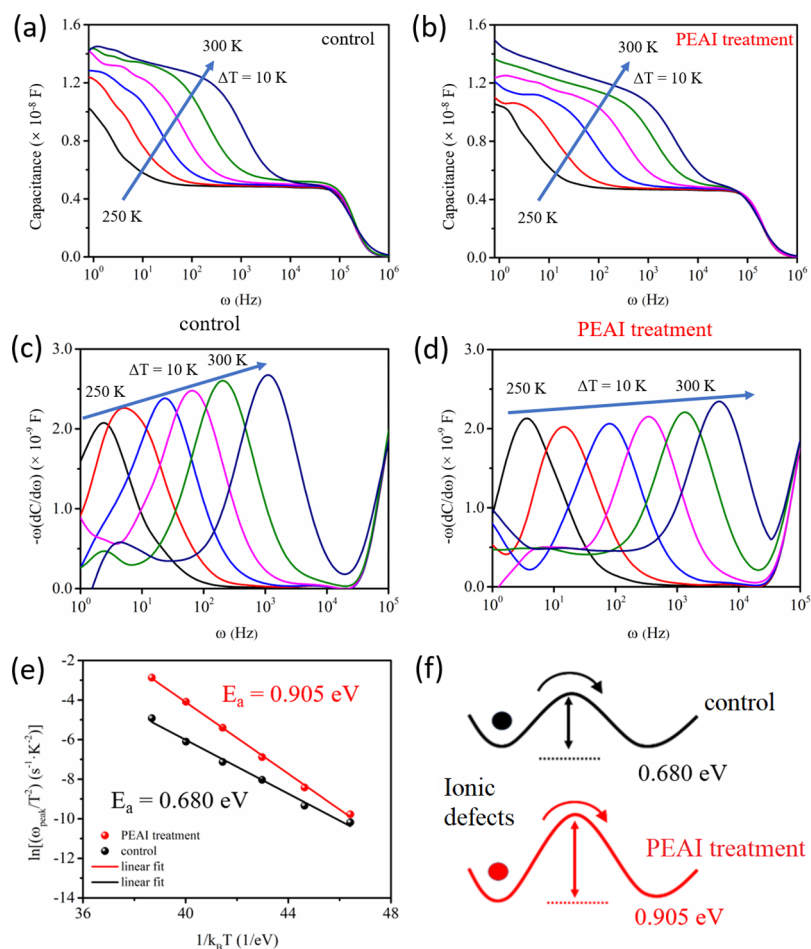
Figure 2. Admittance spectra of WBG PSCs (a) without (the control) and (b) with the PEAI treatment, measured in a temperature range of 250−300 K with a step size of 10 K. Derivatives of the admittance spectra of (c) the control device and (d) the device with the PEAI treatment. (e) Arrhenius plots of the characteristic transition frequencies derived from the admittance spectra. (f) Schematic of the energy barrier for ion movement in the control and the device with PEAI treatment.

the device with the PEAI treatment (Figure S4). As discussed above, a lower n value is typically accompanied by a reduced J_0, which in turn increases the V_{OC} of a solar cell. In a good agreement, the detailed J−V analysis confirms that J_0 is reduced from ∼10^{-10} to 10^{-13} mA/cm^2 with the PEAI treatment (Figure S5). The decreases in J_0 and n contribute to the improvement in V_{OC}, consistent with the prediction (the triangle to star route) in Figure 1h. This decrease in the J_0 and n of the devices after the PEAI treatment is ascribed to the reduction in the microscopic leaking current in GIs and GBs of the WBG perovskite films. The defective GB and defective subsurface region without the PEAI passivation form a poor junction, causing the photoexcited carriers to be transported over the junction via these defects to some degree instead of the desired diffusion process, which subsequently causes energy loss of the charge carriers and reduces the voltage output of the device. It is worth noting that the reduced microscopic leaking current also leads to increased shunt resistance and series resistance (Table S2). However, the change in series resistance has a stronger impact on fill factor (FF) than shunt resistance, leading to a reduced FF. Therefore, the decreased J_0 is the primary reason for the improved performance of PSCs with PEAI treatment.

To further elucidate the interplay between the microscopic and macroscopic currents in the perovskite films and devices,

we conducted TAS measurements on the WBG PSCs without and with the PEAI treatment. We have demonstrated in our recent work that the low-frequency capacitance measured by the TAS technique can be used to estimate the activation energy (E_a) of ionic movement in perovskite absorber layers.[37] Panels a and b of Figure 2 display the TAS spectra of PSCs without and with the PEAI treatment, respectively, measured from 250 to 300 K in the dark. The characteristic transition frequency values (ω_{peak}) were obtained from the derivative of the capacitance−frequency spectra, as shown in panels c and d of Figure 2. Figure 2e shows E_a values calculated by fitting the corresponding Arrhenius plots using the relation $\omega_{peak} = \beta T^2 \exp\left(-\frac{E_a}{kT}\right)$, where β is a temperature-related prefactor.[51] The device with the PEAI treatment exhibits an E_a of 0.905 eV, higher than that of 0.680 eV for the control device. The substantially higher E_a indicates that the ion migration in the perovskite layer is suppressed significantly after the PEAI treatment (Figure 2f). The suppression of mobile ionic defects is also expected to reduce the extent of formation of charge defects that can act as nonradiative recombination centers. We measured the steady-state photo-luminescence (PL) and time-resolved photoluminescence (TRPL) of WBG perovskite films without and with the PEAI treatment (Figure S6). The film with the PEAI treatment
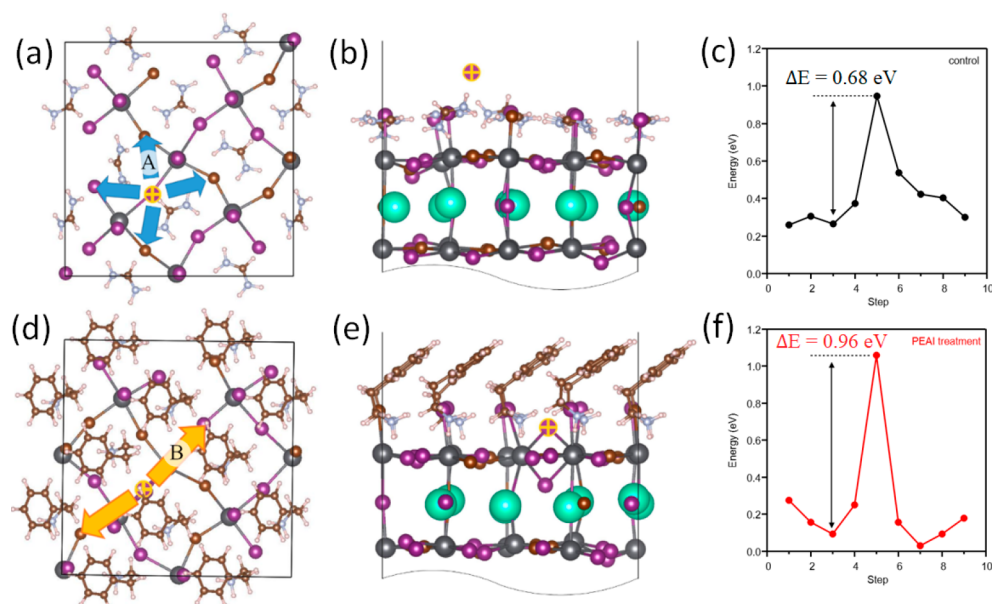
Figure 3. (a) Top view, (b) side view, and (c) energy barrier of the diffusion of the I interstitial on a pristine perovskite surface. Arrow A represents the diffusion path to its nearest site. (d) Top view, (e) side view, and (f) energy barrier of the diffusion of the I interstitial on a PEA-modified perovskite surface. Arrow B represents the diffusion path to the second-nearest site. The purple sphere represents an I atom, and the gray, green, cyan, brown, and white spheres represent Pb, Cs, N, C, and H atoms, respectively. The interstitial I atoms are highlighted.
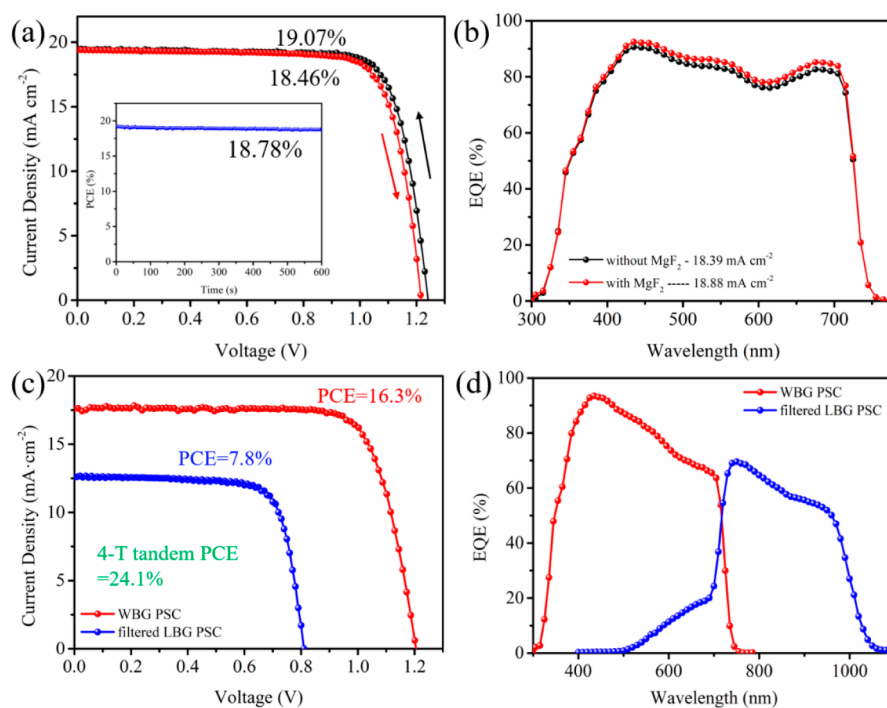
Figure 4. (a) $J-V$ curves of the champion WBG PSC measured under different scan directions. The inset exhibits the stabilized efficiency for the device. (b) EQE spectra of the champion device before and after the deposition of a MgF_2 ARC. (c) $J-V$ curves and (d) EQE spectra of a 4-T all-perovskite tandem cell.

exhibits a more intense PL emission and a longer carrier lifetime compared to those of the control film, demonstrating that PEAI can effectively decrease the rate of nonradiative recombination in WBG perovskite films.

To understand how PEAI can suppress ion migration in perovskites, we performed first-principles calculations to study the behaviors of mobile ionic defects on the surface of perovskite films. It is known that the diffusion and exchange of mobile ions at GBs and on the surface are detrimental to the device performance. Compared to the diffusion in bulk, ions have smaller diffusion barriers on the surface due to smaller steric hindrance. Panels a and b of Figure 3 illustrate the diffusion path of an I interstitial defect loosely bound on the pristine surface. The diffusion of the I interstitial is

accompanied by relatively small geometric distortions, and hance the diffusion barrier. The ion diffusion barrier is calculated to be 0.68 eV (Figure 3c). On the PEA-modified surface, due to the hindrance of PEA, the I interstitial is forced to squeeze into the surface, forming a Pb−I−Pb−I loop (Figure 3d,e), which is similar to the defect structure of an I interstitial in a bulk perovskite (Figure S7). The diffusion barrier of an I interstitial on the PEA-modified surface is increased to 0.96 eV (Figure 3f), suggesting that PEA may help mitigate halide ion migration on the surface. It is worth noting that the finding from the theoretical calculation is in good agreement with the results of TAS measurement. Although the atomic model for the calculation is based on the surfaces of perovskite films, the agreement with the measured diffusion barrier heights indicates that the ETL layer on top of the perovskite film in the devices may have a negligible or minor effect on ion diffusion. Furthermore, the molecular orbital diagram and partial density of states (PDOS) calculations of a PEAI-treated perovskite film (Figure S8) show that an I interstitial introduces a shallow defect level above the valence band maximum, which is similar to the same defect structure on the pristine surface. Therefore, the PEAI treatment does not affect the I interstitial being an innocuous defect.

The aforementioned results combining microscopic conductivity analysis, TAS device analysis, and theoretical calculations indicate that the PEAI surface treatment can suppress ion migration on the surface of perovskite films and prevent the accumulation of ionic defects at GBs. The suppressed ion migration and reduced defective GBs in the near junction region lead to a reduction in the macroscopic J_0. Consequently, the V_{OC} of WBG PSCs increases after the PEAI surface treatment.

Once we understood the effect of PEAI on reducing ion migration and improving the V_{OC} of WBG PSCs, we further analyzed the impact of PEAI concentration on the structural and optical properties of perovskite films and the performance of PSCs. Details are summarized in the Supporting Information (the optimization of PEAI concentration and Figures S9−S15). The optimized PEAI concentration was found to be 2 mg/mL. To further improve the PCE of WBG PSCs, we deposited an antireflection coating (ARC) of MgF_2 to reduce the reflectance of the glass substrate and improve the J_{SC}. Figure 4a shows the $J−V$ curves of the best-performing device with a MgF_2 ARC. The cells show negligible hysteresis and a stabilized efficiency of 18.78%. The J_{SC} gain of ~0.5 mA cm^{-2} due to the MgF_2 ARC is confirmed by the EQE spectra shown in Figure 4b. The increased J_{SC} leads to an improvement in PCE in WBG PSCs from 18.64% to 19.07% (Table S3). To the best of our knowledge, a PCE exceeding 19% is among the highest reported PCEs for inverted WBG PSCs with a bandgap of >1.72 eV (Table S1). The V_{OC} of 1.25 V is remarkable for inverted WBG PSCs. We also fabricated WBG PSCs using a transparent ITO back electrode, yielding a PCE of 16.3% (Figure S16a and Table S4). In addition, the high transmittance beyond 720 nm (Figure S16b) makes it feasible to fabricate efficient perovskite tandem solar cells. As a proof of concept, we combined semitransparent WBG PSCs with a typical 1.25 eV low-bandgap mixed Sn−Pb PSC[46] to construct a 4-T all-perovskite tandem solar cell following a reported approach,[52] demonstrating a PCE of 24.1% (Figure 4c) with complementary spectral responses in both subcells (Figure 4d). This advance shows the promise of high-efficiency all-perovskite tandem solar cells.

In summary, we examined the microscopic and macroscopic origins for the large V_{OC} deficit in the WBG perovskite films and devices and identified that the leaking current of the junction caused by the accumulation of charge defects is one of the major factors limiting the photovoltaic performance of WBG PSCs. We applied an arylammonium surface treatment to suppress ion diffusion to reduce the extent of formation of charge defects on the surface and at GBs. This surface passivation strategy leads to an improvement in the V_{OC} and PCE of WBG PSCs. With electrical and optical optimizations, we demonstrated WBG PSCs with a PCE of 19.07% and a V_{OC} of ~1.25 V, corresponding to a V_{OC} deficit of <0.5 V for a 1.73 eV WBG perovskite absorber layer. Semitransparent WBG cells using an ITO back electrode enabled the creation of 4-T all-perovskite tandem solar cells with PCEs of >24%. This advance in understanding the importance and control of ion migration in WBG perovskites will benefit the development of perovskite tandem solar cells.

■ ASSOCIATED CONTENT

Ⓢ🅘 Supporting Information

The Supporting Information is available free of charge at https://pubs.acs.org/doi/10.1021/acsenergylett.0c01350.

> Experimental section, optimization of the PEAI concentration, reported V_{OC} and PCE values for WBG PSCs, c-AFM of a $MAPbI_3$ film, cross-sectional SEM image of a WBG cell, V_{OC}−light intensity plot for WBG cells, dark saturation current density analysis, PL and TRPL of WBG perovskite films, defect structure of the PEA-modified surface and bulk, molecular orbital diagram and PDOS, SEM images of WBG perovskite films treated with PEAI, AFM topographies of WBG perovskite films, XRD patterns of WBG perovskite films, cross-sectional SEM images of WBG cells, Tauc plots and ultraviolet−visible absorption spectra, $J−V$ and EQE plots for WBG PSCs, statistic distributions of PV parameters, $J−V$, absorption, and reflection spectra of transparent WBG PSCs, PV parameters of PSCs with and without the PEAI treatment, statistics of PV parameters of WBG cells, summary of PV parameters of the best performing cells, PV parameters of cells with and without MgF_2, and PV parameters of transparent PSCs with and without MgF_2 (PDF)

■ AUTHOR INFORMATION

Corresponding Authors

Zhaoning Song − *Department of Physics and Astronomy and Wright Center for Photovoltaics Innovation and Commercialization, The University of Toledo, Toledo, Ohio 43606, United States;* ⓞ orcid.org/0000-0002-6677-0994; Email: zhaoning.song@utoledo.edu

Yanfa Yan − *Department of Physics and Astronomy and Wright Center for Photovoltaics Innovation and Commercialization, The University of Toledo, Toledo, Ohio 43606, United States;* ⓞ orcid.org/0000-0003-3977-5789; Email: yanfa.yan@utoledo.edu

Authors

Cong Chen − *Department of Physics and Astronomy and Wright Center for Photovoltaics Innovation and Commercialization, The University of Toledo, Toledo, Ohio 43606, United States; Key Lab of Artificial Micro- and Nano-*

Structures of Ministry of Education, School of Physics and Technology, Wuhan University, Wuhan 430072, People's Republic of China

Chuanxiao Xiao − National Renewable Energy Laboratory, Golden, Colorado 80401, United States

Rasha A. Awni − Department of Physics and Astronomy and Wright Center for Photovoltaics Innovation and Commercialization, The University of Toledo, Toledo, Ohio 43606, United States

Canglang Yao − Department of Physics and Astronomy and Wright Center for Photovoltaics Innovation and Commercialization, The University of Toledo, Toledo, Ohio 43606, United States

Niraj Shrestha − Department of Physics and Astronomy and Wright Center for Photovoltaics Innovation and Commercialization, The University of Toledo, Toledo, Ohio 43606, United States; orcid.org/0000-0001-5702-2938

Chongwen Li − Department of Physics and Astronomy and Wright Center for Photovoltaics Innovation and Commercialization, The University of Toledo, Toledo, Ohio 43606, United States

Sandip Singh Bista − Department of Physics and Astronomy and Wright Center for Photovoltaics Innovation and Commercialization, The University of Toledo, Toledo, Ohio 43606, United States

Yi Zhang − Department of Physics and Astronomy and Wright Center for Photovoltaics Innovation and Commercialization, The University of Toledo, Toledo, Ohio 43606, United States

Lei Chen − Department of Physics and Astronomy and Wright Center for Photovoltaics Innovation and Commercialization, The University of Toledo, Toledo, Ohio 43606, United States

Randy J. Ellingson − Department of Physics and Astronomy and Wright Center for Photovoltaics Innovation and Commercialization, The University of Toledo, Toledo, Ohio 43606, United States; orcid.org/0000-0001-9520-6586

Chun-Sheng Jiang − National Renewable Energy Laboratory, Golden, Colorado 80401, United States; orcid.org/0000-0003-0230-7500

Mowafak Al-Jassim − National Renewable Energy Laboratory, Golden, Colorado 80401, United States

Guojia Fang − Key Lab of Artificial Micro- and Nano-Structures of Ministry of Education, School of Physics and Technology, Wuhan University, Wuhan 430072, People's Republic of China; orcid.org/0000-0002-3880-9943

Complete contact information is available at:
https://pubs.acs.org/10.1021/acsenergylett.0c01350

Notes
The authors declare no competing financial interest.

■ REFERENCES

(1) NREL Solar Cell Efficiency Chart. https://www.nrel.gov/pv/cell-efficiency.html (accessed 2020-04-26).

(2) Eperon, G. E.; Hörantner, M. T.; Snaith, H. J. Metal Halide Perovskite Tandem and Multiple-Junction Photovoltaics. Nat. Rev. Chem. 2017, 1, 0095.

(3) Lal, N. N.; Dkhissi, Y.; Li, W.; Hou, Q.; Cheng, Y.-B.; Bach, U. Perovskite Tandem Solar Cells. Adv. Energy Mater. 2017, 7, 1602761.

(4) Leijtens, T.; Bush, K. A.; Prasanna, R.; McGehee, M. D. Opportunities and Challenges for Tandem Solar Cells Using Metal Halide Perovskite Semiconductors. Nat. Energy 2018, 3, 828−838.

(5) Song, Z.; Chen, C.; Li, C.; Awni, R. A.; Zhao, D.; Yan, Y. Wide-Bandgap, Low-Bandgap, and Tandem Perovskite Solar Cells. Semicond. Sci. Technol. 2019, 34, 093001.

(6) Duong, T.; Wu, Y.; Shen, H.; Peng, J.; Fu, X.; Jacobs, D.; Wang, E.-C.; Kho, T. C.; Fong, K. C.; Stocks, M.; Franklin, E.; Blakers, A.; Zin, N.; McIntosh, K.; Li, W.; Cheng, Y.-B.; White, T. P.; Weber, K.; Catchpole, K. Rubidium Multication Perovskite with Optimized Bandgap for Perovskite-Silicon Tandem with over 26% Efficiency. Adv. Energy Mater. 2017, 7, 1700228.

(7) Qiu, Z.; Xu, Z.; Li, N.; Zhou, N.; Chen, Y.; Wan, X.; Liu, J.; Li, N.; Hao, X.; Bi, P.; Chen, Q.; Cao, B.; Zhou, H. Monolithic Perovskite/Si Tandem Solar Cells Exceeding 22% Efficiency Via Optimizing Top Cell Absorber. Nano Energy 2018, 53, 798−807.

(8) Han, Q.; Hsieh, Y.-T.; Meng, L.; Wu, J.-L.; Sun, P.; Yao, E.-P.; Chang, S.-Y.; Bae, S.-H.; Kato, T.; Bermudez, V.; Yang, Y. High-Performance Perovskite/Cu(In,Ga)Se$_2$ Monolithic Tandem Solar Cells. Science 2018, 361, 904−908.

(9) Shen, H.; Duong, T.; Peng, J.; Jacobs, D.; Wu, N.; Gong, J.; Wu, Y.; Karuturi, S. K.; Fu, X.; Weber, K.; Xiao, X.; White, T.; Catchpole, K. Mechanically-Stacked Perovskite/CIGS Tandem Solar Cells with Efficiency of 23.9% and Reduced Oxygen Sensitivity. Energy Environ. Sci. 2018, 11, 394−406.

(10) Zhao, D.; Chen, C.; Wang, C.; Junda, M. M.; Song, Z.; Grice, C. R.; Yu, Y.; Li, C.; Subedi, B.; Podraza, N. J.; Zhao, X.; Fang, G.; Xiong, R.-G.; Zhu, K.; Yan, Y. Efficient Two-Terminal All-Perovskite Tandem Solar Cells Enabled by High-Quality Low-Bandgap Absorber Layers. Nat. Energy 2018, 3, 1093−1100.

(11) Al-Ashouri, A.; Magomedov, A.; Roß, M.; Jošt, M.; Talaikis, M.; Chistiakova, G.; Bertram, T.; Márquez, J. A.; Köhnen, E.; Kasparavičius, E.; Levcenco, S.; Gil-Escrig, L.; Hages, C. J.; Schlatmann, R.; Rech, B.; Malinauskas, T.; Unold, T.; Kaufmann, C. A.; Korte, L.; Niaura, G.; Getautis, V.; Albrecht, S. Conformal Monolayer Contacts with Lossless Interfaces for Perovskite Single Junction and Monolithic Tandem Solar Cells. Energy Environ. Sci. 2019, 12, 3356−3369.

(12) Jošt, M.; Bertram, T.; Koushik, D.; Marquez, J. A.; Verheijen, M. A.; Heinemann, M. D.; Köhnen, E.; Al-Ashouri, A.; Braunger, S.; Lang, F.; Rech, B.; Unold, T.; Creatore, M.; Lauermann, I.; Kaufmann, C. A.; Schlatmann, R.; Albrecht, S. 21.6%-Efficient Monolithic Perovskite/Cu(in,Ga)Se2 Tandem Solar Cells with Thin Conformal Hole Transport Layers for Integration on Rough Bottom Cell Surfaces. ACS Energy Lett. 2019, 4, 583−590.

(13) Tong, J.; Song, Z.; Kim, D. H.; Chen, X.; Chen, C.; Palmstrom, A. F.; Ndione, P. F.; Reese, M. O.; Dunfield, S. P.; Reid, O. G.; Liu, J.; Zhang, F.; Harvey, S. P.; Li, Z.; Christensen, S. T.; Teeter, G.; Zhao, D.; Al-Jassim, M. M.; van Hest, M. F. A. M.; Beard, M. C.; Shaheen, S. E.; Berry, J. J.; Yan, Y.; Zhu, K. Carrier Lifetimes of > 1 μs in Sn-Pb Perovskites Enable Efficient All-Perovskite Tandem Solar Cells. Science 2019, 364, 475−479.

(14) Lin, R.; Xiao, K.; Qin, Z.; Han, Q.; Zhang, C.; Wei, M.; Saidaminov, M. I.; Gao, Y.; Xu, J.; Xiao, M.; Li, A.; Zhu, J.; Sargent, E.

H.; Tan, H. Monolithic All-Perovskite Tandem Solar Cells with 24.8% Efficiency Exploiting Comproportionation to Suppress Sn(II) Oxidation in Precursor Ink. *Nat. Energy* **2019**, *4*, 864−873.

(15) Kim, D.; Jung, H. J.; Park, I. J.; Larson, B. W.; Dunfield, S. P.; Xiao, C.; Kim, J.; Tong, J.; Boonmongkolras, P.; Ji, S. G.; Zhang, F.; Pae, S. R.; Kim, M.; Kang, S. B.; Dravid, V.; Berry, J. J.; Kim, J. Y.; Zhu, K.; Kim, D. H.; Shin, B. Efficient, Stable Silicon Tandem Cells Enabled by Anion-Engineered Wide-Bandgap Perovskites. *Science* **2020**, *368*, No. 155.

(16) Xu, J.; Boyd, C. C.; Yu, Z. J.; Palmstrom, A. F.; Witter, D. J.; Larson, B. W.; France, R. M.; Werner, J.; Harvey, S. P.; Wolf, E. J.; Weigand, W.; Manzoor, S.; van Hest, M. F. A. M.; Berry, J. J.; Luther, J. M.; Holman, Z. C.; McGehee, M. D. Triple-Halide Wide−Band Gap Perovskites with Suppressed Phase Segregation for Efficient Tandems. *Science* **2020**, *367*, 1097−1104.

(17) Hou, Y.; Aydin, E.; De Bastiani, M.; Xiao, C.; Isikgor, F. H.; Xue, D.-J.; Chen, B.; Chen, H.; Bahrami, B.; Chowdhury, A. H.; Johnston, A.; Baek, S.-W.; Huang, Z.; Wei, M.; Dong, Y.; Troughton, J.; Jalmood, R.; Mirabelli, A. J.; Allen, T. G.; Van Kerschaver, E.; Saidaminov, M. I.; Baran, D.; Qiao, Q.; Zhu, K.; De Wolf, S.; Sargent, E. H. Efficient Tandem Solar Cells with Solution-Processed Perovskite on Textured Crystalline Silicon. *Science* **2020**, *367*, 1135.

(18) Li, Z.; Kim, T. H.; Han, S. Y.; Yun, Y.-J.; Jeong, S.; Jo, B.; Ok, S. A.; Yim, W.; Lee, S. H.; Kim, K.; Moon, S.; Park, J.-Y.; Ahn, T. K.; Shin, H.; Lee, J.; Park, H. J. Wide-Bandgap Perovskite/Gallium Arsenide Tandem Solar Cells. *Adv. Energy Mater.* **2020**, *10*, 1903085.

(19) Yu, Y.; Wang, C.; Grice, C. R.; Shrestha, N.; Zhao, D.; Liao, W.; Guan, L.; Awni, R. A.; Meng, W.; Cimaroli, A. J.; Zhu, K.; Ellingson, R. J.; Yan, Y. Synergistic Effects of Lead Thiocyanate Additive and Solvent Annealing on the Performance of Wide-Bandgap Perovskite Solar Cells. *ACS Energy Lett.* **2017**, *2*, 1177−1182.

(20) Chen, C.; Song, Z.; Xiao, C.; Zhao, D.; Shrestha, N.; Li, C.; Yang, G.; Yao, F.; Zheng, X.; Ellingson, R. J.; Jiang, C.-S.; Al-Jassim, M.; Zhu, K.; Fang, G.; Yan, Y. Achieving a High Open-Circuit Voltage in Inverted Wide-Bandgap Perovskite Solar Cells with a Graded Perovskite Homojunction. *Nano Energy* **2019**, *61*, 141−147.

(21) Zhou, Y.; Wang, F.; Cao, Y.; Wang, J.-P.; Fang, H.-H.; Loi, M. A.; Zhao, N.; Wong, C.-P. Benzylamine-Treated Wide-Bandgap Perovskite with High Thermal-Photostability and Photovoltaic Performance. *Adv. Energy Mater.* **2017**, *7*, 1701048.

(22) Kim, J.; Saidaminov, M. I.; Tan, H.; Zhao, Y.; Kim, Y.; Choi, J.; Jo, J. W.; Fan, J.; Quintero-Bermudez, R.; Yang, Z.; Quan, L. N.; Wei, M.; Voznyy, O.; Sargent, E. H. Amide-Catalyzed Phase-Selective Crystallization Reduces Defect Density in Wide-Bandgap Perovskites. *Adv. Mater.* **2018**, *30*, 1706275.

(23) Wang, Z.; Lin, Q.; Chmiel, F. P.; Sakai, N.; Herz, L. M.; Snaith, H. J. Efficient Ambient-Air-Stable Solar Cells with 2d−3d Heterostructured Butylammonium-Caesium-Formamidinium Lead Halide Perovskites. *Nat. Energy* **2017**, *2*, 17135.

(24) Tan, H.; Che, F.; Wei, M.; Zhao, Y.; Saidaminov, M. I.; Todorović, P.; Broberg, D.; Walters, G.; Tan, F.; Zhuang, T.; Sun, B.; Liang, Z.; Yuan, H.; Fron, E.; Kim, J.; Yang, Z.; Voznyy, O.; Asta, M.; Sargent, E. H. Dipolar Cations Confer Defect Tolerance in Wide-Bandgap Metal Halide Perovskites. *Nat. Commun.* **2018**, *9*, 3100.

(25) Rajagopal, A.; Stoddard, R. J.; Jo, S. B.; Hillhouse, H. W.; Jen, A. K. Y. Overcoming the Photovoltage Plateau in Large Bandgap Perovskite Photovoltaics. *Nano Lett.* **2018**, *18*, 3985−3993.

(26) Zheng, X.; Chen, B.; Dai, J.; Fang, Y.; Bai, Y.; Lin, Y.; Wei, H.; Zeng, X. C.; Huang, J. Defect Passivation in Hybrid Perovskite Solar Cells Using Quaternary Ammonium Halide Anions And cations. *Nat. Energy* **2017**, *2*, 17102.

(27) Gharibzadeh, S.; Abdollahi Nejand, B.; Jakoby, M.; Abzieher, T.; Hauschild, D.; Moghadamzadeh, S.; Schwenzer, J. A.; Brenner, P.; Schmager, R.; Haghighirad, A. A.; Weinhardt, L.; Lemmer, U.; Richards, B. S.; Howard, I. A.; Paetzold, U. W. Record Open-Circuit Voltage Wide-Bandgap Perovskite Solar Cells Utilizing 2d/3d Perovskite Heterostructure. *Adv. Energy Mater.* **2019**, *9*, 1803699.

(28) Hoke, E. T.; Slotcavage, D. J.; Dohner, E. R.; Bowring, A. R.; Karunadasa, H. I.; McGehee, M. D. Reversible Photo-Induced Trap Formation in Mixed-Halide Hybrid Perovskites for Photovoltaics. *Chem. Sci.* **2015**, *6*, 613−617.

(29) Belisle, R. A.; Bush, K. A.; Bertoluzzi, L.; Gold-Parker, A.; Toney, M. F.; McGehee, M. D. Impact of Surfaces on Photoinduced Halide Segregation in Mixed-Halide Perovskites. *ACS Energy Lett.* **2018**, *3*, 2694−2700.

(30) Gratia, P.; Grancini, G.; Audinot, J.-N.; Jeanbourquin, X.; Mosconi, E.; Zimmermann, I.; Dowsett, D.; Lee, Y.; Grätzel, M.; De Angelis, F.; Sivula, K.; Wirtz, T.; Nazeeruddin, M. K. Intrinsic Halide Segregation at Nanometer Scale Determines the High Efficiency of Mixed Cation/Mixed Halide Perovskite Solar Cells. *J. Am. Chem. Soc.* **2016**, *138*, 15821−15824.

(31) Draguta, S.; Sharia, O.; Yoon, S. J.; Brennan, M. C.; Morozov, Y. V.; Manser, J. S.; Kamat, P. V.; Schneider, W. F.; Kuno, M. Rationalizing the Light-Induced Phase Separation of Mixed Halide Organic−Inorganic Perovskites. *Nat. Commun.* **2017**, *8*, 200.

(32) Knight, A. J.; Wright, A. D.; Patel, J. B.; McMeekin, D. P.; Snaith, H. J.; Johnston, M. B.; Herz, L. M. Electronic Traps and Phase Segregation in Lead Mixed-Halide Perovskite. *ACS Energy Lett.* **2019**, *4*, 75−84.

(33) Jiang, Q.; Zhao, Y.; Zhang, X.; Yang, X.; Chen, Y.; Chu, Z.; Ye, Q.; Li, X.; Yin, Z.; You, J. Surface Passivation of Perovskite Film for Efficient Solar Cells. *Nat. Photonics* **2019**, *13*, 460−466.

(34) Yoo, J. J.; Wieghold, S.; Sponseller, M. C.; Chua, M. R.; Bertram, S. N.; Hartono, N. T. P.; Tresback, J. S.; Hansen, A. C.; Correa-Baena, J.-P.; Bulović, V.; Buonassisi, T.; Shin, S. S.; Bawendi, M. G. An Interface Stabilized Perovskite Solar Cell with High Stabilized Efficiency and Low Voltage Loss. *Energy Environ. Sci.* **2019**, *12*, 2192−2199.

(35) Qian, F.; Yuan, S.; Cai, Y.; Han, Y.; Zhao, H.; Sun, J.; Liu, Z.; Liu, S. Novel Surface Passivation for Stable $FA_{0.85}MA_{0.15}PbI_3$ Perovskite Solar Cells with 21.6% Efficiency. *Solar RRL* **2019**, *3*, 1900072.

(36) Lin, Y.; Chen, B.; Zhao, F.; Zheng, X.; Deng, Y.; Shao, Y.; Fang, Y.; Bai, Y.; Wang, C.; Huang, J. Matching Charge Extraction Contact for Wide-Bandgap Perovskite Solar Cells. *Adv. Mater.* **2017**, *29*, 1700607.

(37) Awni, R. A.; Song, Z.; Chen, C.; Li, C.; Wang, C.; Razooqi, M. A.; Chen, L.; Wang, X.; Ellingson, R. J.; Li, J. V.; Yan, Y. Influence of Charge Transport Layers on Capacitance Measured in Halide Perovskite Solar Cells. *Joule* **2020**, *4*, 644−657.

(38) Ke, W.; Xiao, C.; Wang, C.; Saparov, B.; Duan, H. S.; Zhao, D.; Xiao, Z.; Schulz, P.; Harvey, S. P.; Liao, W.; Meng, W.; Yu, Y.; Cimaroli, A. J.; Jiang, C. S.; Zhu, K.; Al-Jassim, M.; Fang, G.; Mitzi, D. B.; Yan, Y. Employing Lead Thiocyanate Additive to Reduce the Hysteresis and Boost the Fill Factor of Planar Perovskite Solar Cells. *Adv. Mater.* **2016**, *28*, 5214−21.

(39) Shao, Y.; Fang, Y.; Li, T.; Wang, Q.; Dong, Q.; Deng, Y.; Yuan, Y.; Wei, H.; Wang, M.; Gruverman, A.; Shield, J.; Huang, J. Grain Boundary Dominated Ion Migration in Polycrystalline Organic− Inorganic Halide Perovskite Films. *Energy Environ. Sci.* **2016**, *9*, 1752−1759.

(40) Yun, J. S.; Seidel, J.; Kim, J.; Soufiani, A. M.; Huang, S.; Lau, J.; Jeon, N. J.; Seok, S. I.; Green, M. A.; Ho-Baillie, A. Critical Role of Grain Boundaries for Ion Migration in Formamidinium and Methylammonium Lead Halide Perovskite Solar Cells. *Adv. Energy Mater.* **2016**, *6*, 1600330.

(41) Yuan, Y.; Huang, J. Ion Migration in Organometal Trihalide Perovskite and Its Impact on Photovoltaic Efficiency and Stability. *Acc. Chem. Res.* **2016**, *49*, 286−293.

(42) Meggiolaro, D.; Mosconi, E.; De Angelis, F. Formation of Surface Defects Dominates Ion Migration in Lead-Halide Perovskites. *ACS Energy Lett.* **2019**, *4*, 779−785.

(43) Musiienko, A.; Moravec, P.; Grill, R.; Praus, P.; Vasylchenko, I.; Pekarek, J.; Tisdale, J.; Ridzonova, K.; Belas, E.; Landová, L.; Hu, B.; Lukosi, E.; Ahmadi, M. Deep Levels, Charge Transport and Mixed Conductivity in Organometallic Halide Perovskites. *Energy Environ. Sci.* **2019**, *12*, 1413−1425.

(44) Nan, G.; Zhang, X.; Abdi-Jalebi, M.; Andaji-Garmaroudi, Z.; Stranks, S. D.; Lu, G.; Beljonne, D. How Methylammonium Cations and Chlorine Dopants Heal Defects in Lead Iodide Perovskites. *Adv. Energy Mater.* **2018**, *8*, 1702754.

(45) Sherkar, T. S.; Momblona, C.; Gil-Escrig, L.; Ávila, J.; Sessolo, M.; Bolink, H. J.; Koster, L. J. A. Recombination in Perovskite Solar Cells: Significance of Grain Boundaries, Interface Traps, and Defect Ions. *ACS Energy Lett.* **2017**, *2*, 1214−1222.

(46) Li, C.; Song, Z.; Zhao, D.; Xiao, C.; Subedi, B.; Shrestha, N.; Junda, M. M.; Wang, C.; Jiang, C.-S.; Al-Jassim, M.; Ellingson, R. J.; Podraza, N. J.; Zhu, K.; Yan, Y. Reducing Saturation-Current Density to Realize High-Efficiency Low-Bandgap Mixed Tin−Lead Halide Perovskite Solar Cells. *Adv. Energy Mater.* **2019**, *9*, 1803135.

(47) Ye, J. Y.; Tong, J.; Hu, J.; Xiao, C.; Lu, H.; Dunfield, S. P.; Kim, D. H.; Chen, X.; Larson, B. W.; Hao, J.; Wang, K.; Zhao, Q.; Chen, Z.; Hu, H.; You, W.; Berry, J. J.; Zhang, F.; Zhu, K. Enhancing Charge Transport of 2d Perovskite Passivation Agent for Wide-Bandgap Perovskite Solar Cells Beyond 21%. *Solar RRL* **2020**, *4*, 2000082.

(48) Son, D.-Y.; Lee, J.-W.; Choi, Y. J.; Jang, I.-H.; Lee, S.; Yoo, P. J.; Shin, H.; Ahn, N.; Choi, M.; Kim, D.; Park, N.-G. Self-Formed Grain Boundary Healing Layer for Highly Efficient CH₃NH₃PbI₃ Perovskite Solar Cells. *Nat. Energy* **2016**, *1*, 16081.

(49) Cho, K. T.; Grancini, G.; Lee, Y.; Oveisi, E.; Ryu, J.; Almora, O.; Tschumi, M.; Schouwink, P. A.; Seo, G.; Heo, S.; Park, J.; Jang, J.; Paek, S.; Garcia-Belmonte, G.; Nazeeruddin, M. K. Selective Growth of Layered Perovskites for Stable and Efficient Photovoltaics. *Energy Environ. Sci.* **2018**, *11*, 952−959.

(50) Niu, T.; Lu, J.; Jia, X.; Xu, Z.; Tang, M.-C.; Barrit, D.; Yuan, N.; Ding, J.; Zhang, X.; Fan, Y.; Luo, T.; Zhang, Y.; Smilgies, D.-M.; Liu, Z.; Amassian, A.; Jin, S.; Zhao, K.; Liu, S. Interfacial Engineering at the 2d/3d Heterojunction for High-Performance Perovskite Solar Cells. *Nano Lett.* **2019**, *19*, 7181−7190.

(51) Ye, S.; Rao, H.; Zhao, Z.; Zhang, L.; Bao, H.; Sun, W.; Li, Y.; Gu, F.; Wang, J.; Liu, Z.; Bian, Z.; Huang, C. A Breakthrough Efficiency of 19.9% Obtained in Inverted Perovskite Solar Cells by Using an Efficient Trap State Passivator Cu(Thiourea)I. *J. Am. Chem. Soc.* **2017**, *139*, 7504−7512.

(52) Zhao, D.; Wang, C.; Song, Z.; Yu, Y.; Chen, C.; Zhao, X.; Zhu, K.; Yan, Y. Four-Terminal All-Perovskite Tandem Solar Cells Achieving Power Conversion Efficiencies Exceeding 23%. *ACS Energy Lett.* **2018**, *3*, 305−306.